Modeling of the Effect of Path Planning on Thermokinetic Evolutions in Laser Powder Deposition Process

EHSAN FOROOZMEHR and RADOVAN KOVACEVIC

A thermokinetic model coupling finite-element heat transfer with transformation kinetics is developed to determine the effect of deposition patterns on the phase-transformation kinetics of laser powder deposition (LPD) process of a hot-work tool steel. The finite-element model is used to define the temperature history of the process used in an empirical-based kinetic model to analyze the tempering effect of the heating and cooling cycles of the deposition process. An area is defined to be covered by AISI H13 on a substrate of AISI 1018 with three different deposition patterns: one section, two section, and three section. The two-section pattern divides the area of the one-section pattern into two sections, and the three-section pattern divides that area into three sections. The results show that dividing the area under deposition into smaller areas can influence the phase transformation kinetics of the process and, consequently, change the final hardness of the deposited material. The two-section pattern shows a higher average hardness than the one-section pattern, and the three-section pattern shows a fully hardened surface without significant tempered zones of low hardness. To verify the results, a microhardness test and scanning electron microscope were used.

DOI: 10.1007/s11661-010-0561-3

I. INTRODUCTION

LASER powder deposition (LPD) has various applications such as improving the surface properties by coating the surfaces, repairing high-value components, and manufacturing three-dimensional parts. Because usually the spot size of the laser beam is smaller than the deposition area, multiple deposition tracks with a specified overlap ratio are needed to cover the desired area, and several layers have to be deposited to build the desired height of the buildup. The localized cyclic heating and cooling of the part during manufacturing has a serious effect on its final properties. Laser power, laser scanning speed, and powder feeding rate as the main process parameters that can change the macroproperties and microproperties of the material have been studied extensively by several researchers. Kaplan and Groboth[1] studied analytically the effect of the mentioned parameters on the clad layer formation and overlapping of tracks. Labudovic *et al.*[2] studied the effect of process parameters on the formation of residual stress along the height of a single-bead wall deposition. Similar work was performed by Wang and Felicelli,[3] who investigated the effect of the laser power and traverse speed on the material phase transformations during the process. Choi and Chang[4] and Choi and Hua[5] conducted an extensive experimental study on the effect of the laser power, laser scanning speed, and powder flow rate on the geometry, microstructure, and defect formation in the laser cladding of a tool steel. The studies of the process have shown that the microstructure depends not only on the already mentioned parameters but also on any parameter that can change the temperature history of any location throughout the buildup. Costa *et al.*[6,7] studied the effect of idle time between the layers and substrate size[7,8] on the final microstructure and the hardness of the deposition of a single-bead wall. Kelly *et al.*[9] studied the effect of the number of layers in depositing a single-bead wall of titanium alloy on the microstructure evolution. Ghosh and Choi[10–12] studied the residual stress formation during the LPD process by including the microstructural evolutions during the process. Their microstructure evolution model is based on an algorithm developed originally by Watt *et al.*[13] for low-alloy steels to predict the phase transformations of heat-affected zone in weldments. This model describes the formation of ferrite, pearlite, and bainite that are formed in low-to-medium cooling rates, whereas the formation of retained austenite and martensite are considered not to be the purpose of this article. The model developed by Ghosh and Choi,[10–12] however, explains briefly the phase transformation model and does not determine adjustments made to use Watt's model for the LPD process of a high-alloy steel, AISI H13.

An important process parameter that has not been addressed fully yet is the deposition pattern. The authors have shown previously for carbon steel that the deposition pattern can change the final properties of the deposited material significantly.[14] The deposition pattern defines the temperature history of the

EHSAN FOROOZMEHR, formerly PhD Candidate with the Center for Laser Aided Manufacturing (CLAM), Southern Methodist University, Dallas, TX 75275, is now Postdoctoral Fellow with Rapid Prototyping Laboratory, University of Waterloo, Waterloo, Ontario N2L 3G1, Canada. RADOVAN KOVACEVIC, Director of the Center for Laser Aided Manufacturing, Southern Methodist University. Contact e-mail: kovacevi@lyle.smu.edu

Manuscript submitted October 29, 2009.
Article published online December 8, 2010

deposited material and, consequently, affects the phase transformation kinetics of the material. In this article, laser deposition of a hot-work tool steel, AISI H13, with approximately 9 pct alloy elements (0.35 pct C, 5.2 pct Cr, 1.3 pct Mo, 1.0 pct Si, and 1.0 pct V) is modeled. The effect of alloy elements on phase transformation kinetics is considered through a simplified model that can be extended to use for other high-alloy steels.

Solid-state phase transformations are defined by temperature and heating, or cooling rates. In the LPD process of steels, the deposited material consists of the austenite (γ) phase right below the solidus temperature. If the cooling rate is high enough, the martensite transformation occurs, which is a nondiffusive and time-independent transformation (*athermal* transformation). The minimum required cooling rate for transforming austenite to martensite is approximately 20 K/s[15] for AISI H13. Usually, the cooling rate in the LPD process is much higher than 20 K/sec (in the order of 10^4 K/sec,[16]) because of the relatively large cold substrate. Therefore, by crossing the martensite start temperature (M_s), the austenite transforms to martensite until it reaches the martensite end temperature (M_f). If the cooling process stops, the martensite transformation also stops; the martensite continues the transformation only if the temperature continues to cool down.[17] The multipass deposition process disturbs the normal cooling trend of the material and may temper the martensite. Tempering the martensite has four steps: generating transition carbides (373 K to 523 K (100 °C to 250 °C)); transforming retained austenite to ferrite and cementite (473 K to 573 K (200 °C to 300 °C)); replacing the transition carbides with cementite and ferrite (starting from 523 K to 623 K (250 °C to 350 °C)); and forming alloy carbides in the temperature range of 773 K to 923 K (500 °C to 650 °C) for the materials containing a considerable amount of alloy elements such as chromium, titanium, tungsten, molybdenum, and vanadium. The alloy carbides in AISI H13 consist of[14]: M_6C (containing principally molybdenum), M_7C_3 (containing principally chromium), and MC (containing principally vanadium). Alloy carbides have more stability at high temperatures than cementite and maintain or even increase the hardness of the material at high temperatures.[17,18] This rehardening effect at tempering is called *secondary hardening*. At a new heating cycle, the material might have the following three conditions: (1) the material is heated over A_{c3}, the material is fully austenitized, and in the next cooling cycle, the material is transformed to martensite; (2) for temperatures between A_{c1} and A_{c3}, the austenite phase is generated so that it starts from A_{c1} and continues to full austenization at $A_{c3;}$ and (3) for temperatures under A_{c1}, austenization does not occur, and the material is tempered.

In this study, the phase transformation kinetics of AISI H13, hot-work tool steel, is modeled through a coupled finite-element and transformation kinetics model. The model is used to study the effect of dividing the area under deposition into smaller regions on the final microstructure and hardness of the material.

II. FINITE-ELEMENT MODEL OF THE LPD PROCESS

The temperature history at each point in the LPD process defines the phase-transformation kinetics. To solve the problem analytically is either impossible or impractical because of the transient nature of the process and the dependency of the material properties on temperature. ANSYS, Inc. (Canonsburg, PA) finite-element software is used to model the heat transfer numerically during the LPD process. The element "birth and death" option with the aid of ANSYS Parametric Design Language is used to model the additive nature of the process. The temperature history of the nodes at the surface are then transferred to a subroutine developed in the programming language MATLAB (Natick, MA) to analyze the phase transformation and final hardness. The finite-element (FE) model is described briefly here, but more details can be found in Reference 14.

The FE analysis of the temperature of the LPD process with respect to time and location requires the geometry of the part that is defined by a mesh of finite elements updated over time to represent the additive nature of the process. Figure 1 shows the geometry of the finite-element model used in this study, and in a higher magnification, the first set of activated elements on the first bead. The deposition area is 15 × 5 mm, and the spacing between deposition tracks is 0.5 mm. The continuous movement of the laser beam over the substrate is divided into small divisions of the stationary heat transfer analysis, called time steps. In every time step, the energy balance Eq. [1] is solved using the finite-element method, and the results are used as the initial conditions for the next time step.

$$\rho c_p = \nabla \times (k \nabla T) + \dot{q} \qquad [1]$$

In this equation, ρ, k, and c_p are density, thermal conductivity, and specific heat, respectively. $\dot{q}$ is a heat-generation term that is not considered in this model. In every step, a new set of elements is activated. Based on the report by Neto and Vilar,[19] the energy absorbed by flying particles interacting with the laser beam can be sufficient enough to raise their temperature to the melting temperature before reaching the molten pool. Therefore, the new activated elements are assumed to be at their melting temperature. The number of activated elements is equivalent to the volume of the deposited material at the corresponding time step. The boundary conditions are defined initially and updated throughout the process. The substrate is subjected to room temperature as its initial condition. The boundary condition around and on top of the substrate is considered to be convection heat transfer. The bottom of the substrate as suggested by Hu *et al.*[20] and Cho *et al.*[21] is also considered to have convection heat transfer. The laser beam that is assumed to have Gaussian profile is considered as heat flux boundary condition. More details on the elements activation and heat source can be found in Reference 14. The thermal behavior of the material is defined by specifying the temperature-dependent specific heat, thermal conductivity, and density of the material. The latent heat of fusion as suggested by Reference 22 is considered

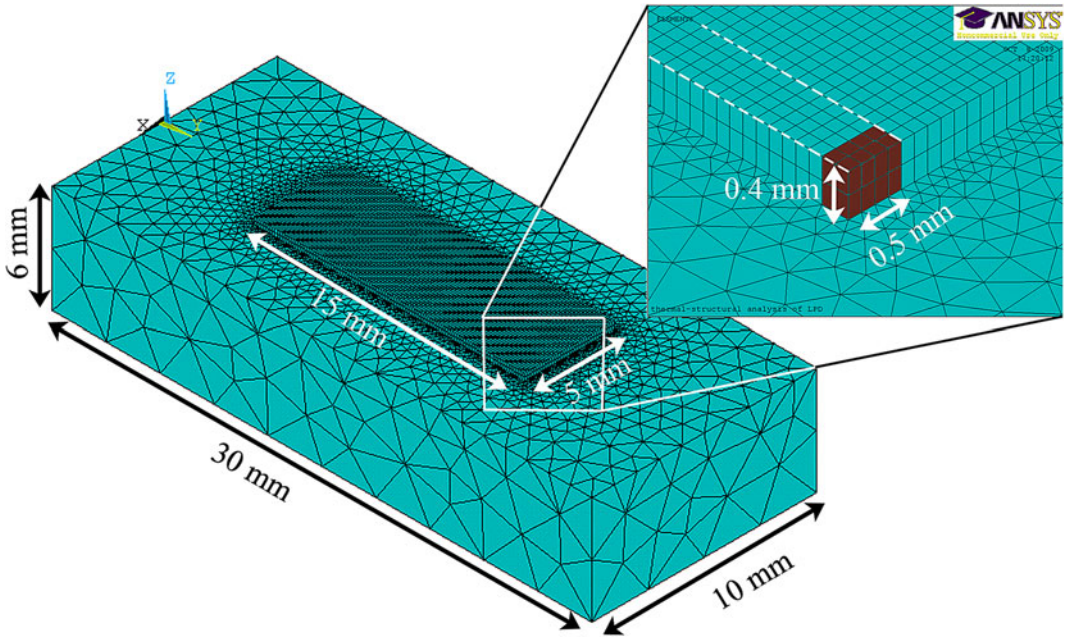

Fig. 1—Finite-element model of the substrate and deposition region for one-layer cladding; the first activated set of elements is shown in a higher magnification.

Table I. Temperature-Dependent Material Properties[22–24]

Temperature [K (°C)]		300 (25)	373 (100)	473 (200)	673 (400)	873 (600)	973 (700)	1073 (800)	1173 (900)	1588 (1315)	1727 (1454)	1873 (1600)
Specific heat (J/kg K)	AISI H13	459	459	518	587	726	905	885	747	905	2014	480
	AISI 1018	454	522	619	789	615	600	615	625	672	1800	844
Density (kg/m^3)	AISI H13	7760	7760	7650	7600	7580	7550	7200	7150	7100	7000	6900
	AISI 1018	7760	7760	7650	7600	7580	7550	7200	7150	7100	7000	6900
Conductivity (W/m K)	AISI H13	17.6	17.6	23	25	26	27	29.5	29.7	30	31	32
	AISI 1018	53.7	49.6	43.3	34.4	29	27	28	28.9	31.6	35	35
Latent heat (kJ/kg)	AISI H13					—					273	—
	AISI 1018					—					245	—

in the definition of specific heat. Table I shows the temperature-dependent material properties of AISI H13.

In the current study, the laser scanning speed is 10 mm/s and the powder feeding rate is 3 g/min with a powder efficiency of 30 pct. The deposition area, as shown in Figure 1, is 15 × 5 mm, and the spacing between deposition tracks is 0.5 mm. With a time step of 25 milliseconds, a set of elements with volume of 0.25 × 0.5 × 0.4 mm^3 is activated (Figure 1). The area on which the heat flux is activated is 0.25 × 0.50 mm^2.

III. THERMOKINETIC MODEL OF THE LPD PROCESS

The thermal analysis of the process results in determining the temperature with respect to time and location. These results are used to predict the phase transformations during the process. The microstructure of the deposited material, just after the solidus temperature, consists of austenite. Depending on the cooling rate of the process, different phases can be developed from the austenite.[25] In the LPD process, the high cooling rate from a large low temperature mass of substrate results in a martensite transformation only when the temperature drops below M_s.[3] The proportion of transformed martensite from the available austenite fraction (f_γ) can be obtained from an empirical relation proposed by Koistinen and Marburger[26]:

$$f_m = 1 - f_\gamma \exp(-0.011(M_s - T))\; M_s > T > M_f \quad [2]$$

where M_s and M_f are martensite start- and end-transformation temperatures, respectively. Although this relation was initially suggested for plain carbon steels, it has shown acceptable results for alloy steels.[27] Obviously, f_γ is equal to 1 for the first cycle. The maximum martensite can be achieved when the material cools down to reach M_f. A small amount of the retained austenite may remain untransformed; the amount would depend on the composition of the material. In the multipass LPD process, the cooling cycle may be disturbed by the next deposited bead that consequently stops the martensite transformation. As mentioned before, depending on the temperature in the new heating cycle, the material structure can be changed.

Reti *et al.*[28] proposed an empirical method to estimate the tempering effect on the medium-carbon, low-alloyed steels. Based on this model, in fully martensitic-quenched steel, the decrease in the Vickers hardness H_m because of tempering at a constant temperature can be expressed as follows:

$$H_m = H_{m0} - B\left(\exp\left(-\frac{Q}{RT}\right)t\right)^n \quad [3]$$

Where H_{m0} is the hardness of the martensite after quenching, and B, Q, and n are empirical constants. For the nonisothermal conditions, Eq. [3] can be written in the following generalized form:

$$H_m = H_{m0} - B\left(\int_0^t \exp\left(-\frac{Q}{RT}\right)dt\right)^n \quad [4]$$

For the alloy steel AISI H13, this method needs to be modified to include the formation of carbides and their effect on hardness. To quantify the parameters B, Q, and n, a series of experiments is performed. In each experiment, two completely quenched samples of AISI H13 are tempered at temperature T to determine the hardness of the corresponding tempering temperature. Based on the least-squares method, the parameters B and n are equal to 1650 and 0.053, respectively. The calculated values of Q at different temperatures are shown in Figure 2. The accuracy of using Eq. [4] to predict the hardness values is shown in Figure 3. As indicated, the calculated values for n, B, and Q provide a close match with the measured values.

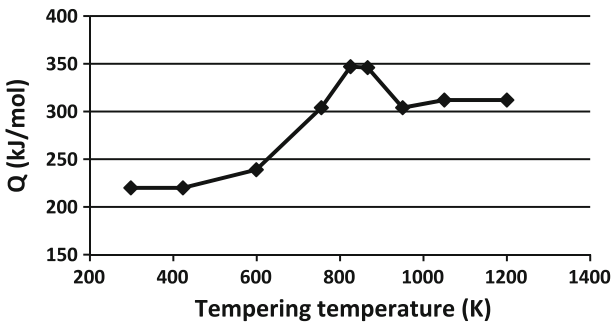

Fig. 2—Q values at different temperatures.

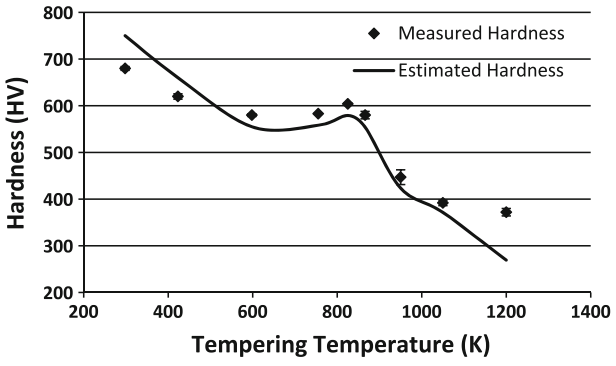

Fig. 3—Comparison of the measured hardness values and the predicted values using the Eq. [4], tempering time = 1 h.

As Figure 3 shows, the temperature-dependent values of the parameter Q result in considering the effect of secondary hardening phenomenon. As indicated in this figure, by tempering the samples from 750 K to 870 K (480 °C to 600 °C), the hardness does not continue the lowering trend and has a peak value in this range. By increasing the tempering temperature, however, the hardness decreases sharply.

The following assumptions are made in the martensite tempering model:

- The tempering process takes place if any fraction of martensite is present.
- The hardness of the tempered martensite is calculated from Eq. [4].
- If the temperature goes higher than A_{c1}, the fraction of austenite linearly increases until it becomes equal to one at A_{c3}.

The final hardness at any point is defined by the following:

$$H = f_{\gamma R} \times H_\gamma + f_m \times H_m \quad [5]$$

where $f_{\gamma R}$ is the retained austenite fraction, H_γ is the hardness of austenite, and f_m and H_m are obtained from Eqs. [2] and [4], respectively. The values of A_{c1}, A_{c3}, and M_s can be estimated from Eq. [6].[17]

$$A_{c1} = 723 - 10.7\text{Mn} + 29.1\text{Si} + 16.9\text{Cr}$$

$$A_{c3} = 910 - 203\sqrt{C} + 44.7\text{Si} + 104V + 31.5\text{Mo} \quad [6]$$

$$M_s = 539 - 423\text{C} - 30.4\text{Mn} - 12.1\text{Cr} - 7.5\text{Mo}$$

However, because of the diffusive nature of the austenization process and by considering the high heating rates in the LPD process (in the order of 10^3 to 10^4 K/s), the transformations occurs at higher temperatures than the ones predicted with Eq. [6].[29] Such hysteresis effect is taken into account by selecting the values of A_{c1} and A_{c3} equal to 1192 K and 1342 K (919 °C and 1069 °C), respectively.[29] Table II summarizes the assumed values in the kinetic model.

Table II. The Assumed Values of the Parameters Used in Modeling of AISI H13

Parameter	Description	Value
A_{c1}	austenization start temperature (K)	1192
A_{c3}	austenization end temperature (K)	1342
B	empirical parameter (HV/s)	1650
H_γ	austenite hardness (HV)	250
H_{m0}	martensite hardness (HV)	750
M_f	martensite transformation end temperature (K)	373
M_s	martensite transformation start temperature (K)	558
n	empirical parameter	0.053
R	universal gas constant (J/mol K)	8.314

IV. THERMOKINETIC-MODEL APPLICATION

Based on the developed thermokinetic model, the effect of path planning on surface modification is studied. The material AISI H13 is used to cover the surface of a substrate of AISI 1018 with three different deposition patterns as shown in Figure 4.

V. RESULTS AND DISCUSSION

The hardness of the surface of the deposited material is calculated for each deposition pattern. To minimize the computational costs of calculations in MATLAB, the nodal solution of the nodes located at the sides of each bead (like along the dashed line shown for the first bead in Figure 1) is taken into account. The results show that the deposition pattern can change the hardness distribution of the deposited material significantly, as a result of changing the heat input. The surface hardness of the one-section pattern, as shown in Figure 5, has a minimum value at the starting bead and a maximum value at the last two beads. In between the starting and ending edges, the hardness has a fairly uniform distribution with a lower value than the maximum hardness.

The surface hardness of the deposition on the two-section pattern is shown in Figure 6. As can be observed, the hardness on the surface has two divisions that represent two steps in the deposition process. The first section is similar to Figure 5 with a slight increase in the hardness of the tempered zone (light color). The second section, however, has a larger area with high hardness (dark color). This area is limited to the last two beads in the first section and to the last four beads in the second section. An area between the two sections is influenced by the deposition process of the second section. This portion is highly tempered by the deposition process of the second section and has a uniform hardness.

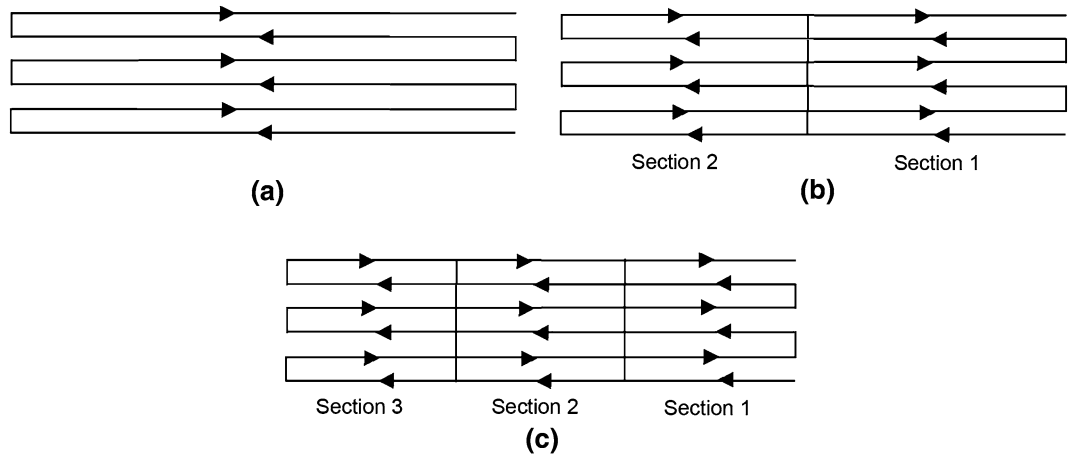

Fig. 4—Schematic presentation of deposition patterns, (*a*) one-section pattern, (*b*) two-section pattern, (*c*) three-section pattern.

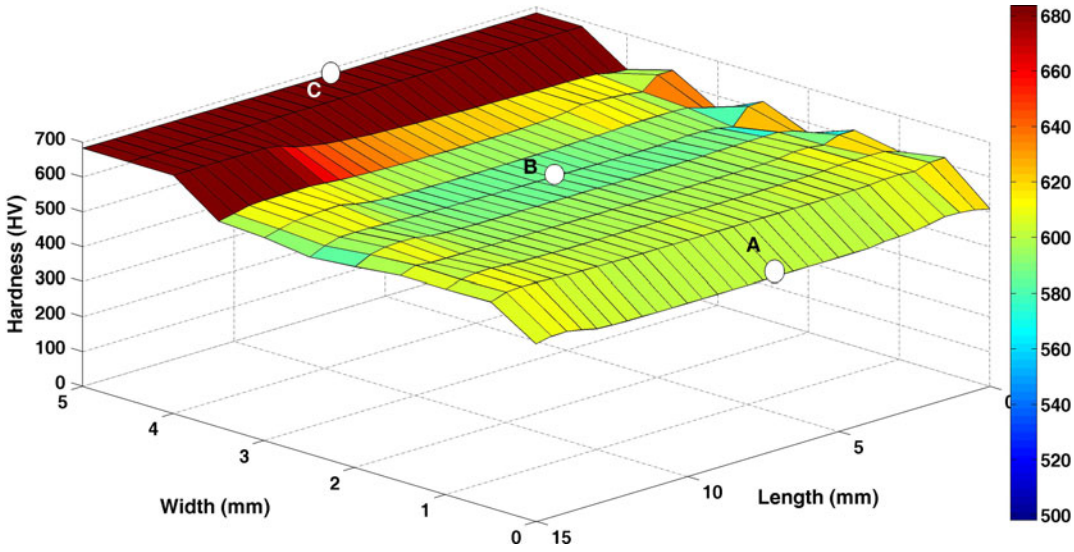

Fig. 5—Surface hardness topography of one-section pattern.

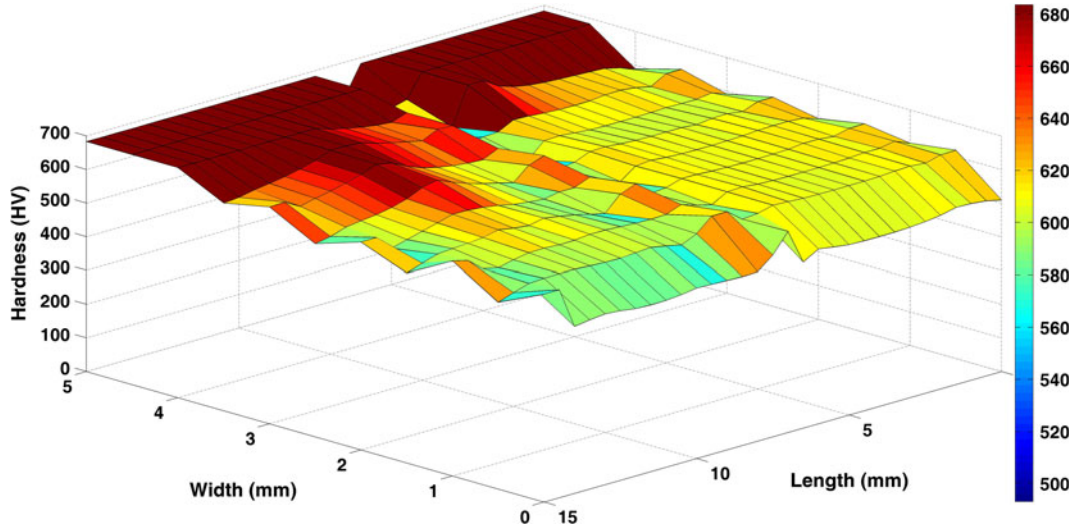

Fig. 6—Surface hardness topography of two-section pattern.

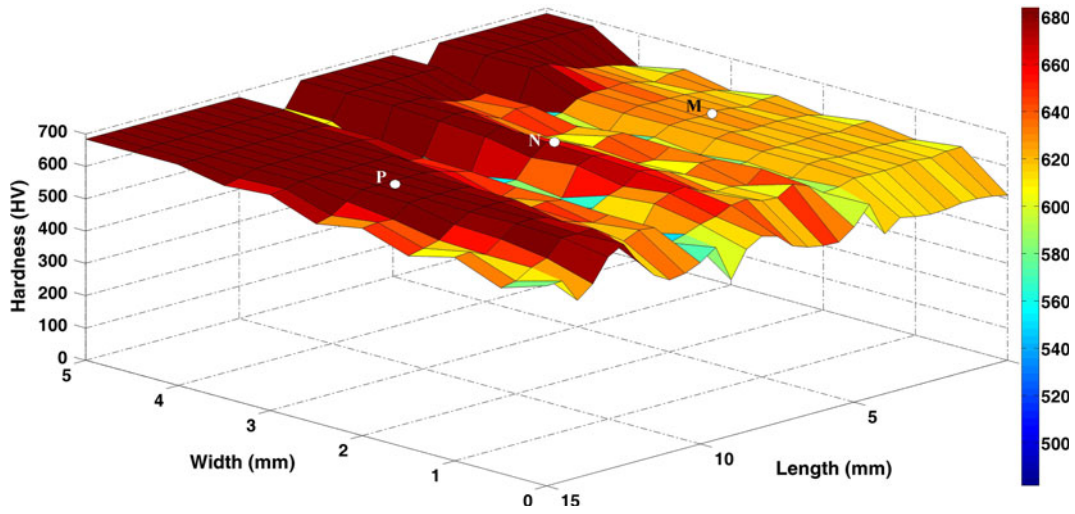

Fig. 7—Surface hardness topography of three-section pattern.

The hardness topography of the three-section pattern is shown in Figure 7. Similar to what was mentioned for the two-section pattern, this topography has three sections. The first section that includes point M has a noticeable higher hardness than the topography of the two-section pattern. The hardness of the second section that includes point N, however, shows much less hardness reduction because of the tempering that takes place with respect to the first section. The hardness in the third section that includes point P is distributed almost uniformly throughout the section. The dark areas in this figure represent the high hardness values. Similar to Figure 6, there are two highly tempered zones in between the sections.

In Figure 8, the corresponding temperature, austenite fraction, and hardness *vs* time for the three points A, B, and C (Figure 5) are described as follows.

The temperature profile for point A shows that the second peak temperature (Figure 8(a), point a) does not cross the A_{c1} line, and a new austenite is not generated (Figure 8(b), point b). The high temperature tempers the material and causes a reduction in the corresponding hardness (Figure 8(c), point c).

The temperature profile for point B shows that the material gets fully austenitized in the first heating cycle continued by a martensite transformation. The second heating cycle also is high enough (Figure 8(a), point i) to austenitize the material fully (Figure 8(b), point j). Consequently, the hardness drops to the austenite hardness level (Figure 8(c), point k). The third peak (Figure 8(a), point m) results in tempering the material and a reduction in the hardness profile (Figure 8(c), point p). Because the maximum tempering temperature for point B (Figure 8(a), point m) is less than the maximum tempering temperature for point A (Figure 8(a), point a), less reduction in hardness is observed (Figure 8(c), point p *vs* point c).

The temperature profile for point C (Figure 8(a)) does not experience any tempering cycle. Therefore, the maximum hardness is expected for this point. It is

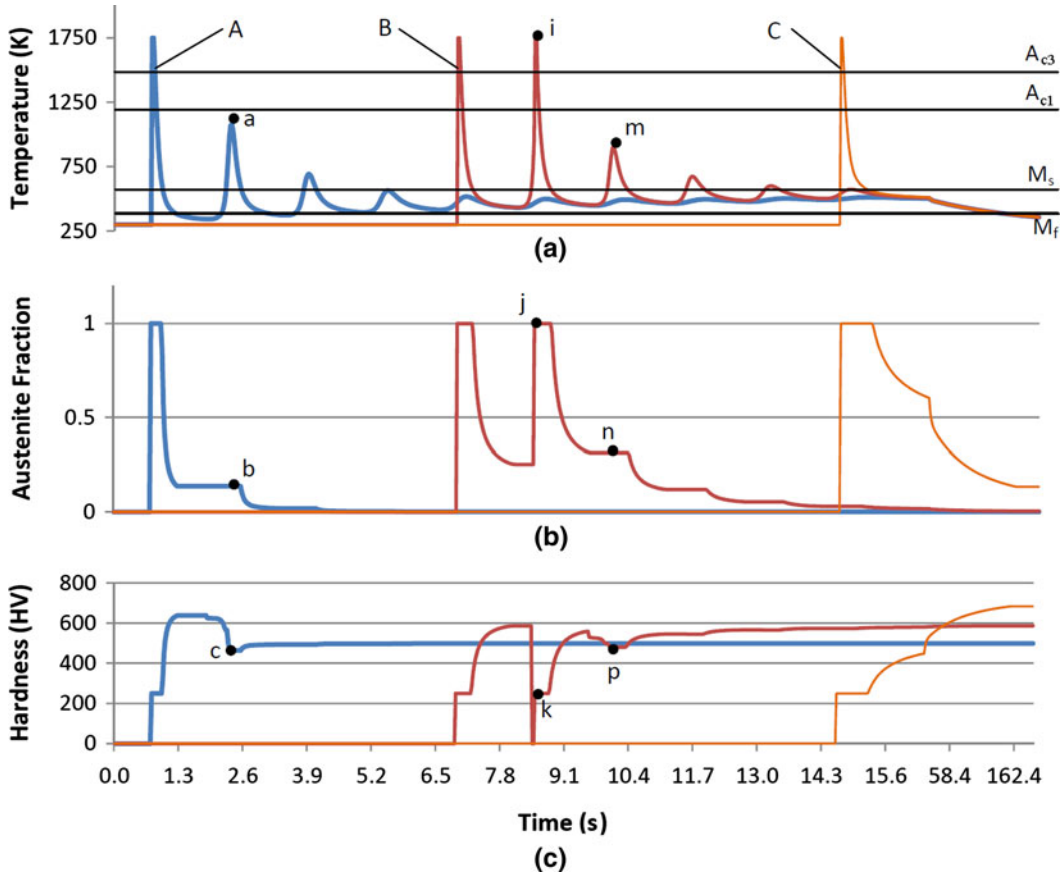

Fig. 8—Temperature (*a*), austenite fraction (*b*), and hardness (*c*) *vs* time for point A (thick line), point B (medium line), and point C (thin line) in Fig. 5.

worth mentioning that the average cooling rate for the point C, which has the smallest value with respect to that of points A and B, is approximately 1500 K/s. This cooling rate is significantly larger than the minimum required cooling rate for martensite transformation for this material, which is 20 K/s.[15]

The retained austenite fraction for points A and B is negligible (Figure 8(b)). However, the retained austenite fraction for point C is approximately 10 pct (Figure 8). This model's prediction of a higher value of retained austenite for untempered locations in the laser deposition process is in agreement with the results reported by Costa *et al.*,[8] Wang and Felicelli,[3] Wang *et al.*,[30] and Colaco and Vilar.[31]

To understand the effect of dividing the deposition area into smaller sections, one point at the center of each section is marked. Points M, N, and P, which are visible topographically in Figure 7, are at the center of the first, second, and third sections, respectively. The temperature, austenite fraction, and hardness of each point *vs* time are graphed in Figure 9. After the second cycle at point M, the material is cooled down to the temperature below M_s (Figure 9(a), point a); the austenite fraction drops to point b (Figure 9(b)), and the hardness increases to point c (Figure 9(c)). The next cycle heats up the material to point i (Figure 9(a)). This cycle tempers the already formed martensite and slightly reduces the corresponding hardness (Figure 9(c), point j). This process continues until point k (Figure 9(a)), in which the heating effect of the deposition of the second section stops the martensite transformation. The rest of the austenite is transformed to martensite when the temperature goes lower than the temperature of point k, that is, point m (Figure 9(a)). This interruption of quenching around M_s results in the stabilization of the retained austenite, which makes the transformation of the austenite into martensite more difficult in the next cooling cycle.[32] This effect, however, is not considered in this model. In the temperature profile of point N (Figure 9), the temperature does not cross the M_s temperature up to the forth thermal cycle. Therefore, no martensite transformation occurs until Figure 9(a), point n. However, for point P, the temperature of any of the thermal cycles does not cross the M_s temperature. Therefore, this point behaves similarly to point C, as shown in Figure 8, and a maximum hardness is achieved.

Comparing the temperature curves of Figure 8 and Figure 9 demonstrates that dividing the deposition area into smaller sections changes the time interval between the thermal cycles. The results can be observed clearly by comparing the austenite fraction of point M after the second peak temperature (Figure 9(b), point b) with the austenite fraction of point A after the first peak

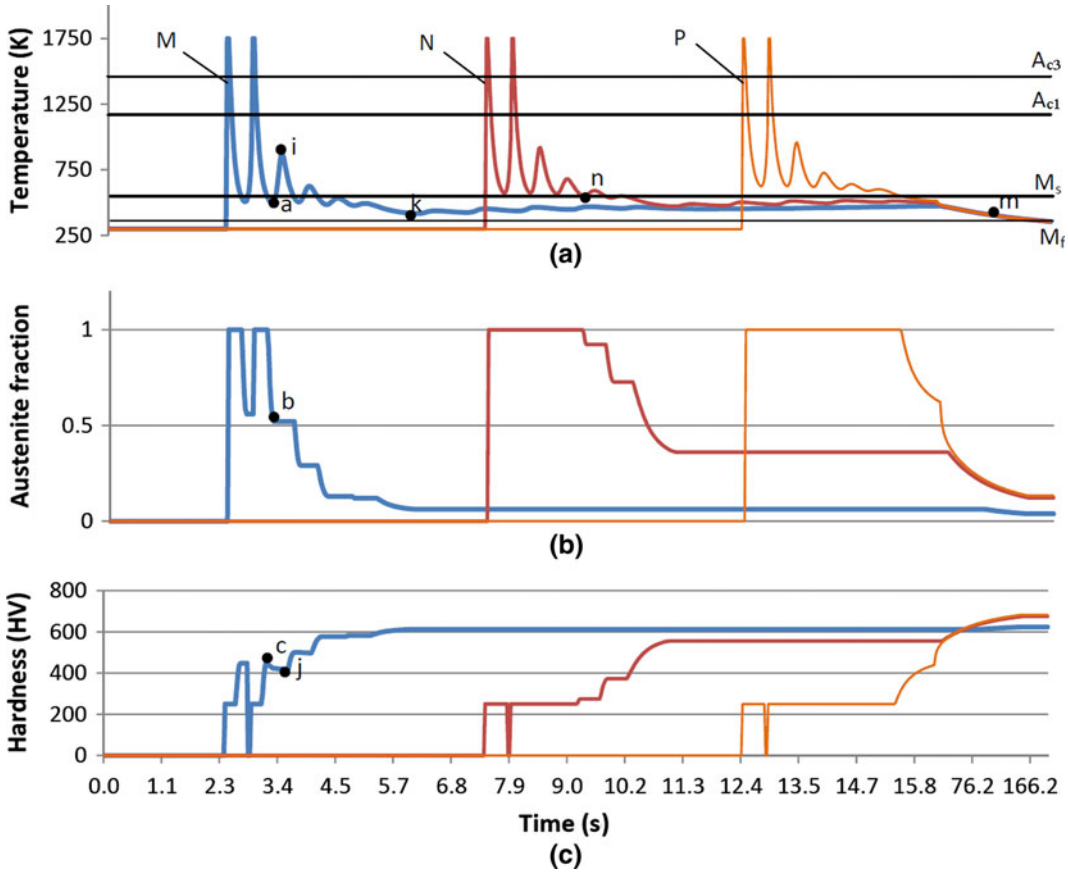

Fig. 9—Temperature (*a*), austenite fraction (*b*), and hardness (*c*) *vs* time, for point P (thin line), point N (medium line), point M (thick line) in Fig. 7.

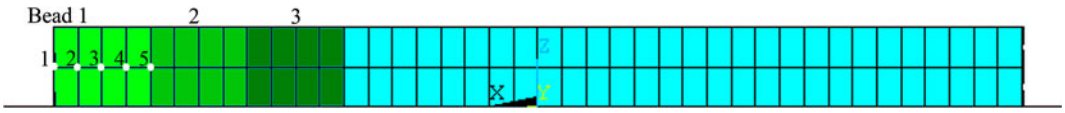

Fig. 10—The location of nodes at the middle of the first bead.

temperature (Figure 8(b), point b). The larger time interval in point A provides enough time for the material even to cross the M_f temperature (Figure 8(a)). Therefore, a large amount of martensite forms and is tempered in the next heating cycle (Figure 8(a), point a). However, as the amount of transformed martensite in point M is less than the one in point A (Figure 9(a)), the hardness reduction (Figure 9(c), point j) is less than the one of point A (Figure 8(c), point c).

As shown, the deposition of each bead results in remelting the mutual side with the previous bead. To have a better understanding of the temperature within one bead, the temperature history of the nodes at the middle of the length and thickness of the first bead (shown with white circles in Figure 10) of the one-section pattern is studied. Figure 11 shows the temperature history of the nodes shown in Figure 10. As can be observed in Figure 11, the effect of the deposition of the second bead on the nodes 1 to 5 is an increase in the temperature in the second heating cycle. This temperature, however, depends on the distance of the node to

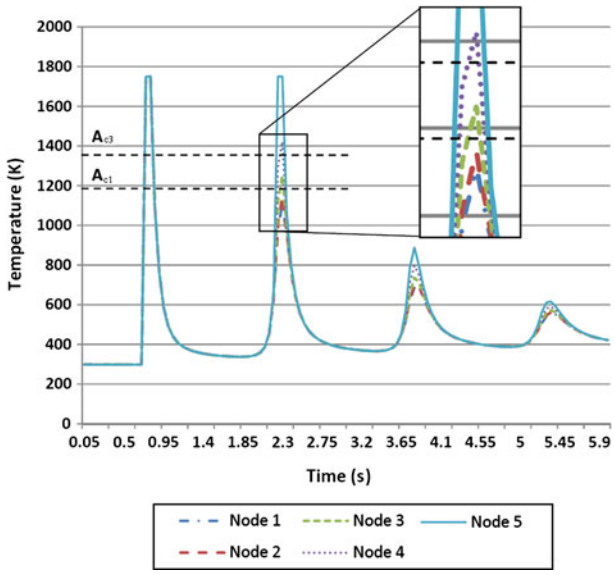

Fig. 11—Temperature history for nodes shown in Fig. 10.

the second bead. For example, node 1 has a minimum increase in temperature, whereas node 5 reaches the melting temperature. The austenization starting and ending temperatures (A_{c1} and A_{c3}) are drawn on Figure 11. As indicated, nodes 4 and 5 are heated over the A_{c3} and are austenitized, whereas nodes 1 and 2 that are below A_{c1} are highly tempered. Node 3, however, is in between A_{c1} and A_{c3} and gets partially austenitized. The third and fourth cycles have a similar trend of temperature variation for the mentioned nodes, but the temperature is below A_{c1} for all nodes. The effect of this temperature variation on the microstructure is discussed subsequently.

VI. MODEL VERIFICATION AND ERROR ANALYSIS

To validate the model and its subsequent conclusions, a series of experiments is performed. The experimental setup comprises a 1-kW continuous wave Nd:YAG laser system with a beam waist radius of 0.5 mm, a five-axis computer numerical control (CNC) vertical machining center, and a powder feeding system with argon carrying gas. Each coupon is clamped on the CNC table before performing the experiment. Each deposition path is defined in the CNC machine with the same process parameters as the model (laser power, laser scanning speed, and spacing between tracks). Figure 12 shows the coupons for different deposition patterns. To compare the surface hardness of the coupons with the modeled hardness values shown in Figures 5 through 7, the top surface of the coupons is ground slightly and polished to become smooth enough for the microhardness test. A 200-g load (making an average indentation size of about 24 μm) and a 150-μm distance between indentations are chosen for the microhardness test experiments. Along the dashed lines shown in Figure 12, two sets of microhardness testing are performed. Line 1 is across the width of the one-section pattern. Lines 2 and 4 are also across the middle of each section of the two-section pattern. Line 3 is along the overlap region of the sections in the two-section pattern. Lines 5, 6, and 7 are also along the middle of each section of the three-section pattern. The results are shown in Figures 13 through 15. The predicted results of hardness are in a good agreement with the measured results. The experimental results obtained in Figure 13 along line 1 show an increase in the hardness of the last two beads. The results in Figure 14(a) along line 2 are similar to the results observed in Figure 13 along line 1. The results in Figure 14(c) along line 4, however, show a larger region with a high hardness. The hardness results in Figure 14(b) along line 3 show a uniform hardness distribution at approximately 590 HV that is related to the effective tempering cycles in this region caused by the deposition of the second section. The measured values of hardness shown in Figure 15 along lines 5, 6, and 7 are close to the values predicted by the thermokinetic model.

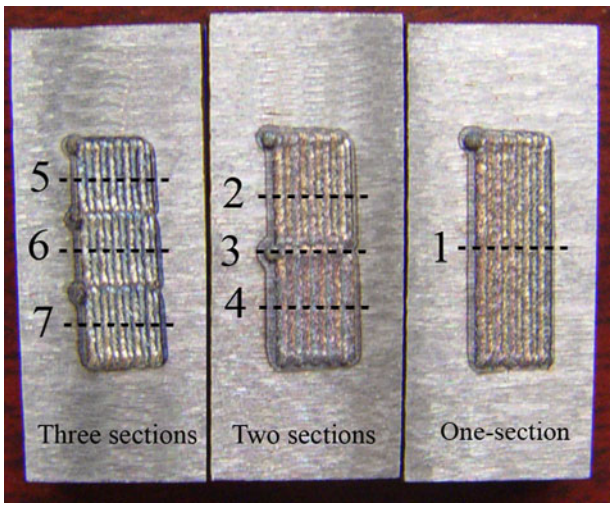

Fig. 12—Experiments performed under different deposition path patterns.

Despite the close match between the predicted hardness values and the experimental results, there is a semiperiodical variation of hardness in the experiments in the regions with low hardness (tempered regions). Figure 16 shows the cross section of the one-section pattern, as shown in Figure 12 along line 1, after polishing and etching with Vilella's reagent. Vilella's reagent is suitable for alloy steels to reveal prior austenite grain boundaries and alloy carbides in quenched martensite and tempered steels.[33] Except the last bead of the shown cross section, other beads, like the shown typical bead, consist of two regions of bright (region 1) and dark (region 2). A higher magnification with scanning electron microscope (SEM) shows a noticeable difference in the microstructure of these two regions (Figure 17). As can be observed in Figure 17(a), the prior austenite grains boundaries can be clearly seen. In addition, some tiny carbides are shown with arrows at the grain boundaries. Figure 17(b), however, shows the carbides in a larger size formed at the grain boundaries. The prior austenite grain boundaries also can be viewed in this figure. The energy dispersive X-ray spectroscopy (EDS) analyses of the two regions on Figure 17(b) are shown in Table III. It is clear that the grain boundary has a larger amount of alloy elements.

Based on the summary of observations shown in Table IV, it can be concluded that the deposition of each bead results in partially reaustenitizing the previously deposited bead up to region 1 (shown in Figure 16 and also Figure 11, nodes 4 and 5) and tempering the

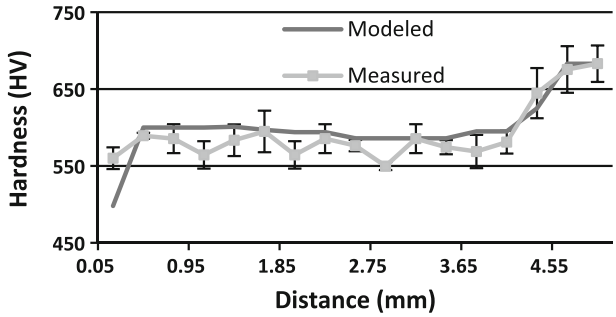

Fig. 13—Measured and predicted hardness along line 1.

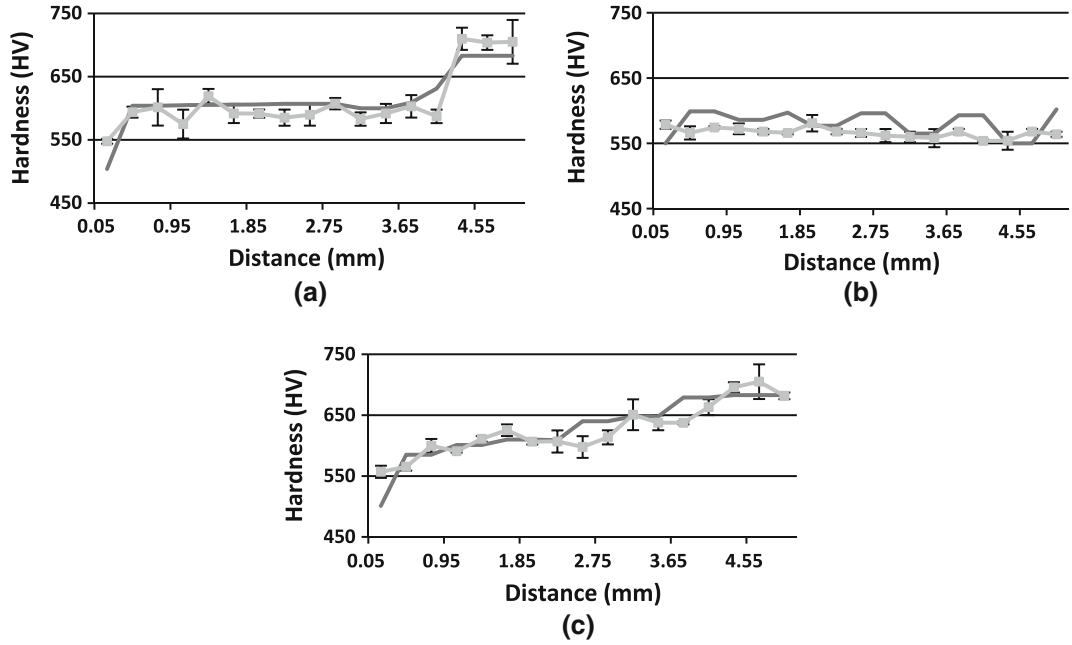

Fig. 14—Measured and predicted hardness of two-section pattern, (*a*) line 2, (*b*) line 3, and (*c*) line 4.

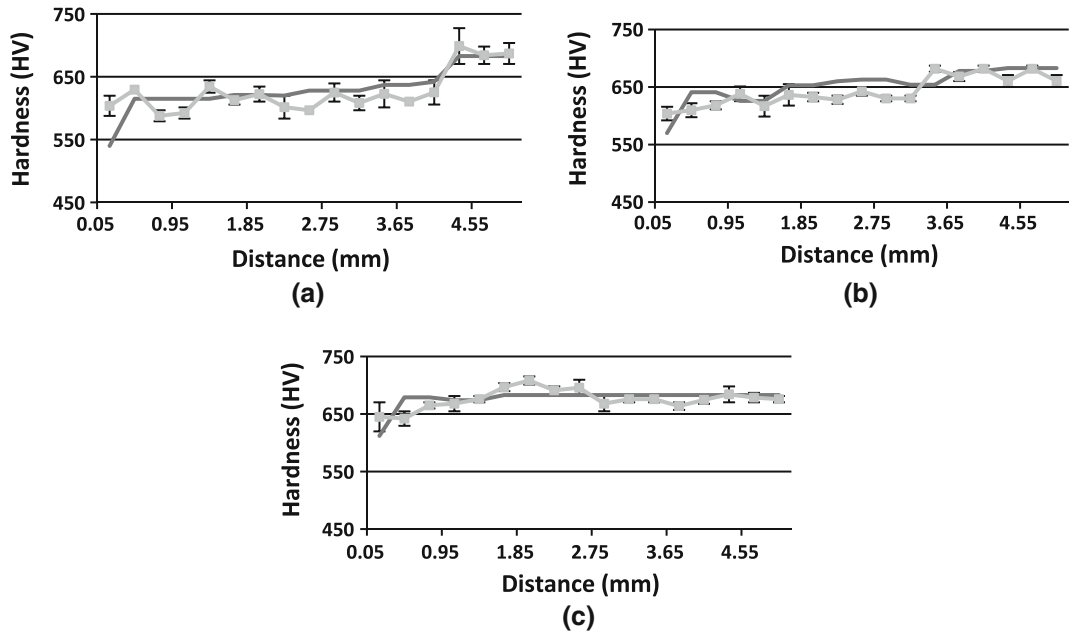

Fig. 15—Measured and predicted hardness of three-section pattern, (*a*) line 5, (*b*) line 6, and (*c*) line 7.

Fig. 16—Cross section of one-section pattern showing regions 1 and 2 in a typical bead.

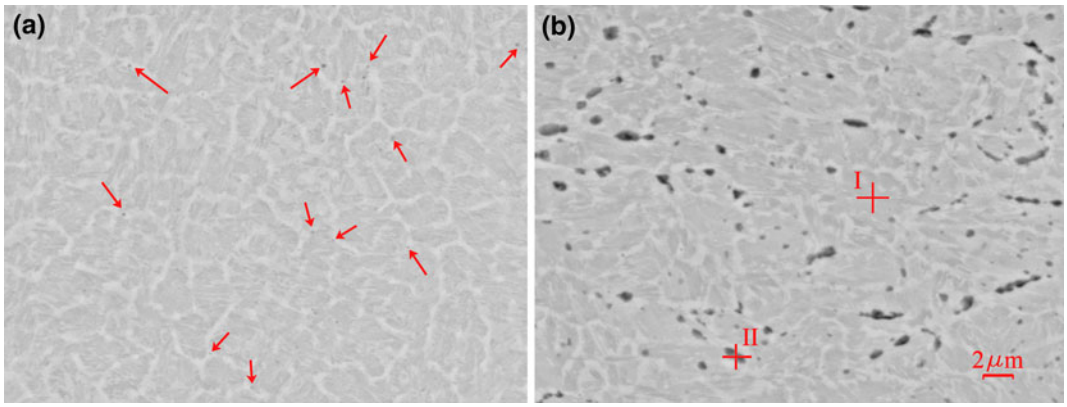

Fig. 17—SEM micrograph of (*a*) region 1 and (*b*) region 2.

Table III. EDS Analysis of Points I and II shown in Fig. 17

	Si	Mo	V	Cr	Fe
Point I (wt pct)	0.96	1.19	0.88	4.47	balanced
Point II (wt pct)	1.08	1.61	1.58	5.06	balanced

Table IV. Summary of Observations

Item	Summary of Observation
Figure 11	depositing a new bead partially austenitizes the previous bead at the mutual edge and tempers the rest of the bead.
Figure 16	the cross section of the one-section pattern shows a typical bead with two regions of dark and bright.
Figure 17(a)	the microstructure of bright region shows the presence of tiny carbides at the grain boundaries.
Figure 17(b)	the microstructure of dark region shows the presence of large carbides at the grain boundaries.
Table III	EDS analysis shows a higher percentage of alloy elements at the grain boundaries.

rest of the bead (shown in Figure 16, region 2, and also Figure 11, nodes 1 and 2). The high temperature in region 2 highly tempers the material and causes the formation and growth of alloy carbides at the grain boundaries. The last bead, however, does not experience any tempering situation.

The variation in microstructure within a tempered bead results in a variation of hardness. To study such local hardness variation, a microhardness test at the cross section of a typical tempered bead is performed. The load applied for the test was 50 g, resulting in an average indentation size of 12 μm, with distance of 75 μm. Figure 18 shows the microhardness test results combined with the cross section of the tempered bead. As can be observed, the hardness in region 1 has higher values than region 2. This shows a severer tempering situation in this region. Nonetheless, the secondary hardening phenomenon (formation of carbides during tempering) maintains the hardness in a reasonably high level. The mentioned variation of hardness across a bead is the reason of the slight mismatch between the model and the experiments shown in Figures 13 through 15 as the data of the nodes within the beads were not taken into account.

Based on the preceding discussion and the presented verifications of the model, the sources of errors involved in this study can be categorized into two groups: errors in the modeling and errors in the experiments. The errors in developing the model are as follows:

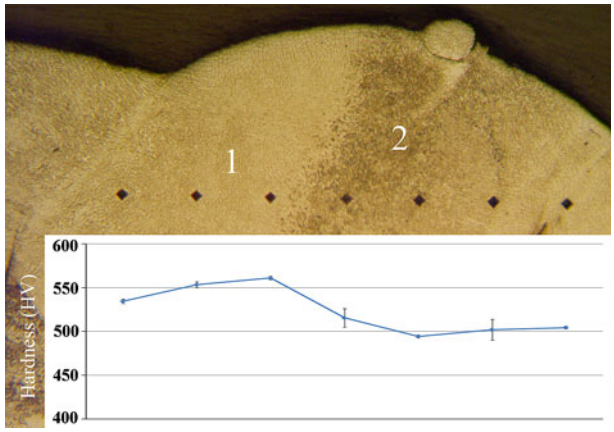

Fig. 18—Microhardness test results at the cross section of a tempered bead.

- Inaccuracies in the material properties
- Ignorance of material convection effect and the dilution with the substrate
- Simplifications in the geometry of the beads and laser beam interaction effects with powder particles

- Errors in calculating the empirical coefficients of n and B

The errors in the experimental verifications are as follows:

- Effect of slightly grinding the surface for microhardness measurements
- Errors in reading the data
- Mismatch between the exact locations that measurements were taken with their corresponding locations in the model

Nonetheless, the overall verification procedure and the close match between the experimental data and the modeling predictions show that the mentioned sources of errors did not have significant effect on the proposed thermokinetic model.

VII. CONCLUSIONS

The use of a multiple-bead LPD process is inevitable for most applications because of the small spot size of the laser beam in comparison with the working area dimensions. Reheating the previous deposited bead results in changing the microstructure and, consequently, changing the mechanical properties of the material. An empirical-based thermokinetic model is developed for AISI H13 to predict the effect of path planning on the final hardness distribution of the coated surface. It is shown that the time interval between the heating cycles that depends on the deposition patterns can influence the phase transformations during the LPD process. When the deposition surface is divided into smaller areas, a higher average of surface hardness can be achieved. The experimental results have a good agreement with the predicted values of the model.

ACKNOWLEDGMENTS

The authors would like to thank Dr. Rouzbeh Sarrafi, Research Engineer in the Center for Laser Aided Manufacturing, for his valuable comments on this study. This work was supported partially by Grant EEC-0541952 from the National Science Foundation.

REFERENCES

1. A.F.H. Kaplan and G. Groboth: *J. Manuf. Sci. Eng. Trans. ASME*, 2001, vol. 123, pp. 609–14.
2. M. Labudovic, D. Hu, and R. Kovacevic: *J. Mater. Sci.*, 2003, vol. 38, pp. 35–49.
3. L. Wang and S. Felicelli: *J. Manuf. Sci. Eng.*, 2007, vol. 129, pp. 1028–34.
4. J. Choi and Y. Chang: *Int. J. Mach. Tool Manuf.*, 2004, vol. 45, pp. 597–607.
5. J. Choi and Y. Hua: *J. Laser Appl.*, 2004, vol. 16-4, pp. 245–51.
6. L. Costa, T. Reti, A.M. Deus, and R. Vilar: *Proc. Int. Conf. Manuf. Sci. Eng*, MPIF, Princeton, NJ, 2002, p. 172.
7. L. Costa, R. Vilar, T. Reti, R. Colaço, A.M. Deus, and I. Felde: *Mater. Sci. Forum*, 2005, vols. 473–474, pp. 315–20.
8. L. Costa, R. Vilar, T. Reti, and A.M. Deus: *Acta Mater.*, 2005, vol. 53, pp. 3987–99.
9. S.M. Kelly, S.S. Babu, S.A. David, T. Zacharia, and S.L. Kampe: *TMS Ann. Meet*, Charlotte, NC, 2004, pp. 45–52.
10. S. Ghosh and J. Choi: *J. Laser Appl.*, 2005, vol. 17-3, pp. 144–58.
11. S. Ghosh and J. Choi: *J. Heat Tran.*, 2006, vol. 128, pp. 662–79.
12. S. Ghosh and J. Choi: *J. Manuf. Sci. Eng.*, 2007, vol. 129, pp. 319–32.
13. D.F. Watt, M. Coon, M. Bibby, J. Goldak, and C. Henwood: *Acta Metall.*, 1988, vol. 36, pp. 3029–35.
14. E. Foroozmehr and R. Kovacevic: *Metall. Mater. Trans. A*, 2009, vol. 40A, pp. 1935–43.
15. G.A. Roberts, G. Krasuss, and R. Kennedy: *Tool Steels*, ASM, Materials Park, OH, 1998.
16. R.S. Lakhkar, Y.C. Shin, and M.J.M. Krane: *Mater. Sci. Eng. A*, 2008, vol. 480, pp. 209–17.
17. M.A. Golozar: *Principles and Applications of Heat Treatment of Steels*, Isfahan Univ. Tech. Press, Isfahan, Iran, 2001.
18. W.F. Smith: *Structure and Properties of Engineering Alloys*, 2nd ed., McGraw-Hill, New York, NY, 1993.
19. O.O.D. Neto and R. Vilar: *J. Laser Appl.*, 2002, vol. 14-1, pp. 46–51.
20. Z. Hu, G. Zhou, and P. Nash: *Modeling of Casting Welding and Advanced Solidification Processes*, XI ed., TMS, Warrendale, PA, 2006, pp. 879–86.
21. C. Cho, G. Zhao, S.Y. Kwak, and C.B. Kim: *J. Mater. Process Technol.*, 2004, vols. 153–154, pp. 494–500.
22. M. Labudovic, D. Hu, and R. Kovacevic: *Proc. Inst. Mech. Eng. Part B J. Eng. Manuf.*, 2000, vol. 214-8, pp. 683–92.
23. S. Zekovic: *Numerical Simulation and Experimental Investigation of Laser-Based Direct Metal Deposition*, UMI Dissertation Services, Ann Arbor, MI, 2006.
24. Y. Lin, K.M. McHugh, Y. Zhou, and E.J. Lavernia: *Metall. Mater. Trans. A*, 2007, vol. 38A, pp. 1632–37.
25. D. Au: Postgraduate Diploma of Research, Auckland University of Technology, Auckland, New Zealand, 2006.
26. D.P. Koistinen and R.E. Marburger: *Acta Metall.*, 1959, vol. 7, pp. 59–60.
27. D. Dean and M. Hidekazu: *J. Comp. Mater. Sci.*, 2006, vol. 37, pp. 209–19.
28. T. Reti, M. Gergely, and P. Tardy: *J. Mater. Sci. Tech.*, 1987, vols. 3–5, pp. 365–71.
29. T. Miokovic, V. Schulze, O. Vohringer, and D. Lohe: *Mater. Sci. Eng. A*, 2006, vols. 435–436, pp. 547–55.
30. L. Wang, H. Kadiri, E. Felicelli, S. Horstemeyer, and M.P. Wang: *SPIE Defense and Security Symposium*, Orlando, FL, 2007.
31. R. Colaco and R. Vilar: *J. Mater. Sci. Lett.*, 1998, vol. 17, pp. 563–67.
32. G.E. Totten and M.A.H. Howes: *Steel Heat Treatment Handbook*, Marcel Dekker Publishers, New York, NY, 1997, pp. 632–33.
33. B.L. Bramfitt and A.O. Benscoter: *Metallographer's Guide, Practices and Procedures for Irons and Steels*, ASM, Materials Park, OH, 2002.